

1 **Critically testing olivine-hosted putative Martian biosignatures in the Yamato 000593**  
2 **meteorite - geobiological implications**

3

4 **Abstract:**

5 On rocky planets such as Earth and Mars the serpentinization of olivine in ultramafic crust  
6 produces hydrogen that can act as a potential energy source for life. Direct evidence of fluid-rock  
7 interaction on Mars comes from iddingsite alteration veins found in Martian meteorites. In the  
8 Yamato 000593 meteorite putative biosignatures have been reported from altered olivines in the  
9 form of microtextures and associated organic material that have been compared to tubular  
10 bioalteration textures found in terrestrial sub-seafloor volcanic rocks. Here we use a suite of  
11 correlative, high-sensitivity, in-situ chemical and morphological analyses to characterize and re-  
12 evaluate these microalteration textures in Yamato 000593, a clinopyroxenite from the shallow sub-  
13 surface of Mars. We show that the altered olivine crystals have angular and micro-brecciated  
14 margins and are also highly strained due to impact induced fracturing. The shape of the olivine  
15 microalteration textures is in no way comparable to microtunnels of inferred biological origin  
16 found in terrestrial volcanic glasses and dunites, and rather we argue that the Yamato 000593  
17 microtextures are abiotic in origin. Vein filling iddingsite extends into the olivine microalteration  
18 textures and contains amorphous organic carbon occurring as bands and sub-spherical  
19 concentrations <300 nm across. We propose that a Martian impact event produced the micro-  
20 brecciated olivine crystal margins that reacted with subsurface hydrothermal fluids to form  
21 iddingsite containing organic carbon derived from abiotic sources. These new data have  
22 implications for how we might seek potential biosignatures in ultramafic rocks and impact craters  
23 on both Mars and Earth.

24 **Key words:** biosignatures, serpentinization, impact events, hydrothermal-synthesis, organic  
25 carbon.

26

## 27 **1. Introduction:**

28 Ultramafic rocks containing olivine and pyroxenes are a major component of the  
29 lithosphere of early terrestrial planets and are altered in the presence of water to produce serpentine  
30 minerals (Muntener 2010). Hydrogen is released during serpentinization and is widely thought to  
31 be critical for the emergence of life, because it acts as an energy source for metabolism (e.g. Kelley  
32 et al. 2005; Russell, 2007). The subsurface of Mars has been postulated to provide a sizeable  
33 potential habitat for life supported by the interaction of liquid water with the mafic crust (Fisk and  
34 Giovannoni 1999, Schulte et al. 2006) and numerous candidate biosignatures have been suggested  
35 in these environments (e.g. Grosch et al. 2014). Rover missions and remote sensing surveys have  
36 documented abundant evidence for liquid water in near surface environments on Mars (Mustard  
37 2008; Bishop et al. 2008; Squyres et al. 2012) and identified evidence for aqueous alteration of the  
38 crust, for example, in hydrothermal systems associated with impact craters (Ehlmann et al. 2011),  
39 and groundwater upwelling zones (Michalski et al. 2013). Direct evidence of the low-temperature  
40 aqueous alteration of the martian subsurface is found in the Nakhla group of meteorites that contain  
41 hydrous minerals such as carbonates, clays, opal-A and iron oxides, collectively referred to as  
42 iddingsite (Changela and Bridges 2011; Bridges and Schwenzer 2012; Lee et al. 2015). Evidence  
43 for life in the form of textural and chemical biosignatures in these meteorites is much more  
44 tentative, with putative reports coming from Nakhla (Fisk et al. 2006), Yamato 000593 (White et  
45 al. 2014) and Tissint (Lin et al. 2014) - although none of these have been widely accepted. Here  
46 we will further investigate the evidence found in Yamato 000593.

47           The alteration of terrestrial seafloor volcanic glass and ultramafic dunites has been  
48 explored as an analogue for identifying potential microbial alteration of the martian crust by  
49 several workers (e.g. Fisk et al. 2006; Grosch et al. 2014; McLoughlin and Grosch 2015; Turke et  
50 al. 2015). A study by Fisk et al. (2006) was the first to tentatively propose evidence of possible  
51 bioerosion in olivines of the Nakhla meteorite, in which they reported micron sized tunnels  
52 emanating from iddingsite filled fractures in the olivine (fig. 4 of Fisk et al. 2006), although these  
53 authors emphasize that a biogenic origin has not been conclusively demonstrated for either the  
54 terrestrial or martian microtunnels. More recently a study by White et al. (2014) reported putative  
55 indigenous organics in the meteorite Yamato 000593, comprising small spheres of carbon less than  
56 500 nm across embedded in the iddingsite, which were tentatively suggested to be microbial in  
57 origin. The study also described microtextures at the interface between the olivine crystals and  
58 iddingsite alteration that were described as microtubular in shape and compared to microtunnels  
59 of inferred microbial origin found in terrestrial seafloor volcanic glasses. Here we will investigate  
60 these microtextures and associated organics at higher magnification and evaluate the biogenicity  
61 of these candidate martian biosignatures.

62           In this study we investigate the meteorite Yamato 000593 (henceforth Y000593) which is  
63 the largest fragment at 13.7 kg of a meteorite fall found near the Yamato Mountains in Antarctica  
64 that also includes the Yamato 000749 (1.28 kg) and Yamato 000802 (0.022 kg) meteorites. On the  
65 basis of mineralogical studies and noble gas analysis Y000593 has been classified as belonging to  
66 the Nakhlite subgroup of martian meteorites and is believed to be derived from a sill like body that  
67 formed <100m beneath the Martian surface (Mikouchi et al. 2003). Y000593 is a cumulate igneous  
68 rock termed a clinopyroxenite containing c. 80% coarse grained augite, c. 10% coarse grained  
69 olivine and c. 10% mesostasis (fine-grained interstitial material comprising plagioclase, pyrrhotite,

70 apatite, fayalite, tridymite and magnetite). The meteorite contains a single generation of fractures  
71 cross cutting the igneous grains that are filled with iddingsite alteration, which are estimated to  
72 occupy 4% volume of the olivines (Changela and Bridges 2010) and give a brownish appearance  
73 to the olivines. Y000593 has a surface that is c. 60% covered by a black fusion crust formed during  
74 atmospheric entry that is observed to both truncate the veins of iddingsite alteration, and in some  
75 instances also melts these veins near the fusion crust (Treiman and Goodrich 2002). Based on these  
76 observations it has been argued that the iddingsite alteration formed prior to atmospheric entry and  
77 is pre-terrestrial in origin (Treiman and Goodrich 2002, White et al. 2014). Radiometric dating has  
78 found that Y000593 has an Amazonian crystallization age of  $1310 \pm 30$  million years (Shih et al.  
79 2002) and that the fracture filling iddingsite alteration yields Rb-Sr ages of  $633 \pm 23$  Ma interpreted  
80 as the age of aqueous alteration on Mars (Borg and Drake 2005). Several studies of the composition  
81 and distribution of the aqueous alteration phases in the Nakhilites have argued for an origin from  
82 ephemeral subsurface hydrothermal alteration in impact craters on Mars (Changela and Bridges  
83 2011; Bridges and Schwenzer 2012; Lee et al. 2015). Subsequently, Yamato and the co-magmatic  
84 Nakhlite meteorites were ejected from Mars by a large impact event that is estimated to have  
85 occurred c. 11 million years ago (Eugster et al. 2002).

86 Here we use focused ion beam (FIB) milling combined with transmission electron  
87 microscopy (TEM) enabling us to document at high-magnification the altered olivine crystals and  
88 associated alteration products in Y000593. In particular, we aim to document the morphology of  
89 the interface between the olivine and alteration products and to see if there is a progressive  
90 alteration front in the olivine crystals, thereby exploring the mechanism of olivine dissolution and  
91 alteration. In addition, we use a suite of high spatial resolution and high sensitivity spectroscopic  
92 techniques [TEM-EDS; electron energy loss spectroscopy (EELS); and nano-scale secondary ion

93 mass spectrometry (NanoSIMS)] to characterize the distribution and ultrastructure of the organic  
94 carbon. We will use correlated C, N and Cl mapping to document if there is more than one  
95 generation of organic carbon, and to test for potential contamination derived from terrestrial  
96 sources, including sample preparation. TEM-EELS data will also allow us to characterize the  
97 bonding environment of the organic carbon and attached functional groups, to document for  
98 example, whether the carbon comprises crystalline graphite, or amorphous carbon and therefore  
99 explore possible sources for the organics. Our combined data will further test the origins of the  
100 olivine microalteration textures in Y000593, the source of the organic carbon, and whether either  
101 is relevant to seeking potential biosignatures on Mars.

102

## 103 **2. Material and Methods:**

### 104 2.1 Petrography and Scanning Electron Microscopy (SEM)

105 The Yamato meteorite sample was studied in a standard polished petrographic thin section (30µm  
106 thick) and as a polished chip using light microscopy and SEM to identify areas of interest (Fig. 1).  
107 This material is on loan from the Japanese polar institute. Optical images were obtained using a  
108 Nikon LV100Pol polarizing microscope and photographed using a DS-Fi1 color camera with 5.24-  
109 megapixel resolution coupled to NIS-Elements BR 2.30 software. A Zeiss Supra 55VP SEM at the  
110 University of Bergen, Norway was used to investigate the Ir coated samples in secondary electron  
111 (SE) and backscatter electron (BSE) mode. Elemental analysis was conducted using an attached  
112 Thermo Noran Six EDS system to obtain element spot analyses and qualitative maps of the  
113 elements of interest.

114

### 115 2.2 Focused Ion Beam (FIB) preparation and Transmission Electron Microscopy (TEM)

116 Ultra-thin lamellas for TEM analysis were prepared by FIB milling, using a dual-beam FEI Helios  
117 Nanolab 600. Electron beam imaging was used to identify target areas in the polished thin section,  
118 allowing site-specific TEM samples to be prepared. Two protection layers were always deposited  
119 on the sample surface prior to cutting out the TEM lamellas: A thin Pt layer was first deposited  
120 with electron beam assisted deposition to avoid any ion beam damage at the sample surface. A  
121 thicker Pt protection layer (ca. 2  $\mu\text{m}$  thick) was deposition on top of the e-beam Pt by ion beam  
122 assisted deposition. The sizes of the TEM lamellas are ca.  $8 \times 10 \mu\text{m}$  across and 50-150 nm thick.  
123 They were lifted out and transferred to *Omniprobe* Cu TEM grids using an in-situ technique where  
124 a W lift-out needle is used to transfer the TEM lamella onto the grid, with ion-beam assisted Pt  
125 deposition used to weld the sample to the lift-out needle and to Cu posts on the TEM grid. Coarse  
126 thinning was performed at 30 kV ion beam acceleration voltage and with progressively lower beam  
127 current, finishing with 90 pA current. Further thinning was performed at 5 kV and 73 pA, before  
128 the final polishing at 2 kV and 17 pA.

129 Three lamellas were analyzed at the TEM Gemini Centre at NTNU by a double Cs corrected  
130 (probe- and image-corrected) cold-FEG JEOL ARM 200CF, operated at 200 kV. The ARM is  
131 equipped with a large solid angle (0.98 srad solid angle) Centurio SDD for X-ray Energy  
132 Dispersive Spectroscopy (EDS) and a fast Gatan Quantum ER with Dual-EELS (energy electron  
133 loss spectroscopy). Simultaneous EDS and EELS mapping was performed in STEM (scanning  
134 transmission electron microscopy) mode i.e. each pixel in every map contains one EDS and two  
135 EEL spectra. Based on the position of the zero loss peak, the low loss EEL spectrum was used to  
136 calibrate the energy scale in the core loss spectrum in every pixel. EEL spectra were collected with  
137 a 380 pA beam current and with semi-convergence and semi-collection angles of 27 and 66 mrad,  
138 respectively. Spectra taken to construct element maps were recorded with 1 eV/channel and 3 eV

139 energy resolution. Mapping of the C peak was done with 0.1 eV/channel and 0.57 eV resolution  
140 (based on the FWHM of the zero loss peak), and the semi-collection angle was reduced from 66  
141 to 33 mrad. Prior to inserting the FIB lamellas into the TEM, all samples were plasma cleaned  
142 using a gas mixture of 75% Ar and 25% O<sub>2</sub> for 2 min to remove all possible hydrocarbon  
143 contamination on the sample surfaces.

144 TEM image processing was conducted in the GATAN Digital Micrograph© software (64 bit  
145 DM 2.32.888.0). The intensities of the EDS and EELS bitmap files are qualitative and show  
146 relative variations inside the mapped regions. The selected area electron diffraction patterns were  
147 collected in TEM mode with a parallel beam. The diffraction patterns of unknowns were calibrated  
148 by diffraction patterns (taken under identical conditions) from a Si single crystal with known lattice  
149 parameters. The EEL spectra were also processed in Digital Micrograph©. The energy was  
150 calibrated from semi-simultaneously acquired low-loss spectra that included the zero loss peak. A  
151 standard power law function was used to subtract the background intensity.

152

### 153 2.3 Nano-scale secondary ion mass spectrometry (NanoSIMS)

154 NanoSIMS mapping of the polished chip embedded in a 25 mm epoxy ring was performed using  
155 a CAMECA NanoSIMS 50 at the Centre for Microscopy, Characterisation and Analysis (CMCA)  
156 at the University of Western Australia. A Cs<sup>+</sup> primary ion beam was rastered across analysis areas  
157 varying from 5 x 5 µm up to 20 x 20 µm, at a resolution of 256 x 256 pixels (each pixel measuring  
158 between 20 nm and 78 nm, depending on the size of the area imaged). Dwell times were 20 ms per  
159 pixel with a primary beam current of c. 2.8 pA (D1=2), 30 ms per pixel with a beam current of c.  
160 1.3 pA (D1=3) and 45 ms per pixel in 'high resolution mode' using a c. 0.7 pA beam current  
161 (D1=4). Secondary ions mapped were <sup>16</sup>O<sup>-</sup>, <sup>24</sup>C<sub>2</sub><sup>-</sup>, <sup>12</sup>C<sup>14</sup>N<sup>-</sup>, <sup>32</sup>S<sup>-</sup> and <sup>56</sup>Fe<sup>16</sup>O<sup>-</sup>, and charge

162 compensation was achieved by using the electron flood gun. Nitrogen does not form secondary  
163 ions so the  $CN^-$  complex was used to map nitrogen distribution. In all cases, regions c. 2-5  $\mu m$   
164 larger than the intended analysis area were pre-sputtered with the primary ion beam (using c. 250  
165 pA beam current;  $D1=1$ ) to  $> 5 \times 10^{16}$  ions/cm<sup>2</sup> in order to remove surface contamination, implant  
166  $Cs^+$  ions and reach a steady-state of ion emission. In order to discount any potential contribution  
167 from epoxy resin in our results we present ion maps from potential organic material as  $^{12}C^{14}N^-$   
168  $/^{24}C_2^-$ . Measurements of this ratio from the resin in which the rock chip was mounted resulted in a  
169  $^{12}C^{14}N^-/^{24}C_2^-$  of 0.5 +/- 0.1. In contrast, the  $^{12}C^{14}N^-/^{24}C_2^-$  for organic material within the targeted  
170 alteration microtextures is at least an order of magnitude greater (mostly between c. 15 and 25).  
171 Hence, while resin is frequently present in fractures close to the microtextures of interest it cannot  
172 be responsible for the high  $^{12}C^{14}N^-/^{24}C_2^-$  signals observed within specific microtextures. Analyses  
173 were performed on both the surface of a polished rock chip and on a TEM lamella extracted from  
174 below the surface of the rock chip. The TEM lamella for NanoSIMS was prepared using a FEI  
175 Helios G3CX dual beam instrument at CMCA following a similar procedure to that described  
176 above for the Nanolab 600 instrument.

177

### 178 **3. Results:**

179 The optical light microscopy images of Y000593 (Fig. 1 a-c) show curving fractures,  
180 especially around the margins of the olivine grains, filled with red-brown iddingsite alteration,  
181 which at higher magnification show apparent linear features propagating into the olivines  
182 (arrowed, Fig. 1c). The iddingsite shows an angular, “spikey” interface with the fresh olivine when  
183 observed by SEM (Fig. 1e and Fig. 2) and TEM (Fig 1f). There are two phases of alteration clearly  
184 seen in Fig 1d and Fig 2: a central more compact and amorphous phase (white arrows in Fig. 1d



185 and f, termed iddingsite 1) that is more-dense and often shows a distinct central band, and an outer  
186 more porous and partially crystalline phase (black arrows in Fig. 1d and f, termed iddingsite 2)  
187 that rims the veins and penetrates along high-angle fractures into the olivines (Fig. 1d, arrowed).  
188 SEM-EDS mapping shows that the inner iddingsite phase is relatively Si enriched (black arrow in  
189 Si panel of Fig. 2) and the outer phase more Fe enriched (white arrow in Fe panel of Fig. 2), the  
190 iddingsite sometimes contracts due to dehydration during sample preparation and pulls away from  
191 the margins of the veins. TEM investigation reveals that the angular and micro-brecciated olivine  
192 crystal margins (Fig. 1 f-h) contain a high degree of strain and a significant defect density shown  
193 by the dark bands and complex contrast variation recorded in the bright field TEM images (Fig.  
194 1g and h).

195 FIB milling was used to obtain electron transparent TEM lamellae orientated parallel,  
196 orthogonal and oblique to the margins of the iddingsite-filled veins at the locations shown in Fig.  
197 3. During FIB milling a “saw tooth” interface was revealed between the olivine and the alteration  
198 products, both on the sample surface (Fig. 3c) and beneath (Fig. 3d arrow), again confirming the  
199 angular nature of these interfaces. Selected area electron diffraction (SAED) by TEM confirms  
200 that the olivines are single crystals (Fig. 3) and have lattice parameters ( $a=4.84 \text{ \AA}$   $b=10.38 \text{ \AA}$   
201  $c=6.08 \text{ \AA}$ ) close to the Fe-rich fayalite end member ( $a=4.82 \text{ \AA}$   $b=10.47 \text{ \AA}$   $c=6.10 \text{ \AA}$ ), with very  
202 minor Mg also evident in chemical maps (Fig. 2). The vein-filling iddingsite phase is rather  
203 variable in composition. It is commonly amorphous but where it does show crystallinity the  
204 diffraction patterns plus the chemical mapping suggests the presence of smectitic clay (e.g.,  
205 nontronite; Fig. 3) and small amounts of goethite (Fig. 3). The amorphous iddingsite is relatively  
206 Si enriched, whereas the outer more crystalline iddingsite is more Fe enriched (Fig. 2).  
207 Comparisons of the  $^{32}\text{S}^-$ ,  $^{56}\text{Fe}^{16}\text{O}^-$  and  $^{16}\text{O}^-$  NanoSIMS maps (e.g. Figs. 4,5 and S1), plus some of

208 the TEM-EDS maps (see below and Figs. 6-8) suggests the presence of a Fe-sulphate phase within  
209 the alteration products. In all cases the margins of the olivine crystals can be seen to break down  
210 into small fragments (Fig. 1e and h, 4,5) and the iddingsite phase penetrates into the olivine crystals  
211 along high-angle fractures (Fig. 3-8). This records a progressive alteration front between the  
212 olivines and iddingsite-filled veins that is angular in shape.

213 NanoSIMS ion mapping reveals elevated concentrations of organic material as sub-micron  
214 sized areas in the outer iddingsite phase close to the olivine interface (Figs. 4, 5 and S1). This  
215 organic material has a distinctive CN/C signal ( $> 10$ ) that is at least an order of magnitude greater  
216 than the CN/C signal ( $< 1$ ) from epoxy resin in which the sample is mounted (Fig. 4,5 and S1).  
217 This discounts resin as a source of the organics that are intimately associated with the olivine  
218 interface. The CN/C signal does not provide any information on the concentration of N in the  
219 organic material since we have no way of standardising this measurement, but rather as a relative  
220 comparison between the mounting resin and potentially indigenous organics. The location of the  
221 high CN/C organics close to and within the micro-brecciated olivine crystal margins suggest that  
222 they are related to micro-brecciation and early alteration of the olivine crystals and iddingsite  
223 formation. The organics appear unrelated to primary magmatic features such as inclusions and  
224 zoning in the olivines.

225 To further characterize the morphology, distribution and structure of the organic carbon  
226 that is intimately associated with the angular microalteration textures, TEM-EDS and EELS were  
227 employed. TEM images of FIB-milled cross sections through the alteration textures show that the  
228 organic carbon occurs as rare patches  $< 300$  nm across, especially in the outer vein-filling iddingsite  
229 phase 2 (Figs. 6-8). Area a shown in Fig. 6 shows bands of carbon along the margins of the  
230 iddingsite filled vein and occurring in fractures that penetrate deep into the host olivine crystals.

231 Area b (noted on Fig. 6 and shown at higher resolution in Fig. 7), also from the outer iddingsite  
232 phase, contains bands of carbon within the iddingsite plus smaller patches of carbon at the roots  
233 of the olivine-penetrating microfractures. Some of these patches suffer from FIB induced damage  
234 whereby differential rates of thinning particularly between organics and minerals results in small  
235 sub-spherical holes so potentially there were even greater volumes of carbon present prior to FIB-  
236 milling, e.g., Fig 8a. arrow. A further area mapped from a different FIB lamellae shown in Figure  
237 8 reveals significant carbon located near to an angular olivine crystal margin. In all mapped regions  
238 the organic carbon distribution does not correlate with enrichments in Ca or O and is therefore not  
239 associated with a carbonate phase. There is no correlation of C with the Ga or Pt TEM-EDS maps,  
240 excluding contamination during FIB wafer preparation. We looked in several regions to check that  
241 the C and Cl EDS maps do not correlate (Fig. 6-8), also that no Cl peak is seen in the EDS or EELS  
242 spectra so that we can exclude possible glue/resin used in attaching the thin section to the glass  
243 slide as a source for the organics. In contrast, we found that in one FIB-lamella cut from the epoxy-  
244 embedded rock chip that was prepared for nanoSIMS ion mapping (and subsequently discarded),  
245 there was a correlation between the C and Cl in the TEM-EDS maps (Supplementary Fig. S2). In  
246 that case we interpret the C to be derived from the epoxy located in what was void space. We  
247 therefore conclude that the correlation between C and Cl TEM-EDS maps is an additional reliable  
248 way to check for possible contamination from epoxy during sample preparation, and that we thus  
249 have two robust methods (C and Cl correlation, plus CN/C ratio) to distinguish this from  
250 primary/indigenous sources of organic material. (Note, this NanoSIMS combined elemental  
251 mapping approach has previously been used to distinguish microbial organics found in fragments  
252 of seafloor volcanic glass from epoxy (McLoughlin et al. 2011), and the current study is the first  
253 to employ this approach to FIB lamellae mapped using both NanoSIMS and TEM-EDS.)

254 EELS spectra measured from organic bearing regions in Fig. 6 (red boxes) exhibit a carbon-  
255 K near edge structure very similar in shape to reference spectra derived from amorphous carbon  
256 (Fig. 9a), with a distinct but less intense  $\pi^*$  peak at  $\sim 285$  eV and a broader more intense  $\sigma^*$  peak  
257 centered around 295 eV (Fig. 9b). The C-K near edge structure lacks the distinct  $1s \rightarrow \sigma^*_1$  exciton  
258 at  $\sim 292$  eV that characterizes crystalline graphite found in meteorites (Cody et al. 2008). The  $1s$   
259  $\rightarrow \pi^*$  electronic transition at  $\sim 285$  eV indicates a significant amount of C=C bonding, most likely  
260 polyaromatic domains (Bernard et al. 2010) while the broad, rather featureless  $\sigma^*$  peak centered  
261 around 295 eV indicates a lack of long range order in these domains (Garvie and Busek 2006).  
262 There appear to be small additional peaks in the 287-290 eV range that have been attributed in  
263 previous studies to either, stacking defects between the aromatic planes, or carboxylic functional  
264 groups due to partial oxidation of the sample (Bernard et al. 2010). Our samples do not show the  
265 sharp peaks at about 290 eV and 301 eV that indicate carbonate groups (Fig. 9a) and also lack the  
266 triplet of distinct peaks (at about 293, 298 and 305 eV) characteristic of high pressure phases such  
267 as diamond (Fig. 9a) that have previously been identified in meteorites (Garvie and Busek 2006)  
268 and lunar impact melts (Steele et al. 2010).

269

## 270 **4. Discussion:**

### 271 4.1 Nature and origin of the Y000593 microalteration textures.

272 The FIB-TEM data reported here enables us to examine at high magnification and in 3-  
273 dimensions the microalteration textures found in the olivines of the Y000593 meteorite. We find  
274 that the interface between the olivines and iddingsite alteration is angular and micro-brecciated in  
275 morphology (Fig. 1, 3) with a network of iddingsite filled fractures occurring between angular  
276 olivine fragments (Fig. 1-8). The altered olivines show a “saw tooth” interface between fragmented

277 olivine crystal margins and the iddingsite alteration (Fig. 1-3). We find no tunnel-like features in  
278 our FIB-TEM images, neither in cross nor longitudinal section. We see no similarity in shape to  
279 microtunnels of inferred biological origin found in terrestrial volcanic glass and dunites.  
280 Summarising previous morphological studies of terrestrial bioalteration textures, the microtunnels  
281 are typically 1-6  $\mu\text{m}$  wide, up to hundreds of micrometers long, and can be curving, twisted or  
282 even helical in shape (c.f. Fisk and McLoughlin 2013 and references therein). The terrestrial  
283 bioalteration tunnels occur in bands radiating at high angles from fractures in the glass, often co-  
284 occurring with spherical or so called granular alteration textures (Furnes et al. 2001). The Yamato  
285 microtextures are on average shorter in length, and rather than being microtunnel-shaped, are  
286 angular interconnected fractures that do not co-occur with spherical-etch pits or granular  
287 microtextures. We therefore reject the comparison to terrestrial bioalteration textures and a  
288 microbial origin for the microtextures found in olivine grains of Y000593 as suggested by White et  
289 al. (2014).

290 We highlight that the size, shape and distribution of the Y000593 olivine microalteration  
291 textures is also very different to etch pits produced by the terrestrial weathering of olivines (Velbel  
292 2009, 2016). For example, a study of the nakhalite meteorite Miller Range (MIL) 03346 found  
293 notches and serrations along fractures in olivine grains, showing conical and biconical  
294 morphologies (figures 5-8 of Velbel 2016) that are concentrated within a few hundred microns of  
295 the meteorite's fusion-crust, supporting an origin from terrestrial weathering. These triangular or  
296 wedge shaped etch pits are up to 2 $\mu\text{m}$  long, can occur as diamond shaped pairs, or echelon arrays  
297 following dislocations in the olivines (figure 1 Velbel 2016). The smaller aspect ratio and  
298 triangular shape of these olivine terrestrial weathering textures distinguishes them from the much  
299 more elongate microtextures that we imaged in the olivines of Y000593 (Figs 1-5).

300 Our brightfield TEM images (Fig. 1g and h) show evidence of shock induced strain in the  
301 olivine crystals, recorded by the significant defect density shown by the dark bands and complex  
302 contrast variation (Fig. 1g and h). We therefore suggest that impact event(s) were responsible for  
303 creating the angular fracture network we observe in the Y000593 olivines that were subsequently  
304 aqueously altered. Previous studies have argued that the relatively low peak shock state of the  
305 nakhlites estimated at 20 GPa (Nyquist et al., 2001) is consistent with their location near the  
306 margins of a Martian impact crater, rather than being in the center of the crater.

307

#### 308 4.2 Nature of the Y000593 iddingsite alteration and organics

309 The iddingsite alteration veins investigated here in Y000593 are pre-terrestrial in origin  
310 because they are truncated by the fusion crust (Treiman and Goodrich 2002). (In contrast a  
311 terrestrial weathering overprint is seen in Yamato Y000749 where small cracks and bubbles occur  
312 in the fusion crust (Treiman and Goodrich 2002) that is also cross-cut by terrestrial jarosite veins  
313 (Changela and Bridges 2010)). The Fe-rich fayalitic olivine compositions we measure (Fig. 3) are  
314 comparable to previous studies of the mineralogy of Yamato 000593 (Imae et al. 2003) and the  
315 Nakhilites more broadly (table 4 in Treiman 2005), and consistent with Fe-rich iddingsite alteration  
316 products found, as opposed to more Mg-rich clays/serpentinites. Several studies of the Nakhilites  
317 have shown that heat derived from an impact event caused melting of the Martian permafrost and  
318 formation of a hydrothermal system in an impact crater with aqueous alteration and iddingsite  
319 formation (e.g., Changela and Bridges 2011; Bridges and Schwenzer 2012; Chatzitheodoridis et  
320 al. 2014). Thermochemical modelling based on the mineral alteration assemblages observed  
321 suggests an initially CO<sub>2</sub>-rich hydrothermal fluid at temperatures between 150 and 200 °C, with a  
322 water: rock ratio (W/R) ≤ 300, with a pH of 6–8 leading to Fe-carbonate precipitation, followed

323 by a fluid that cooled to temperatures of 50 °C, at a pH of 9 giving rise to Fe-rich phyllosilicate  
324 and serpentine precipitation, then formation of amorphous Si-rich gel (Bridges and Schwenzer  
325 2012). Yamato being the shallowest of the Nakhla meteorites contains iddingsite that comprises  
326 largely a siderite-gel assemblage. The organic carbon found in Y000593 is thus located in the  
327 relatively low-temperature part of an impact generated hydrothermal system, with several potential  
328 sources for the organics.

329 The organic carbon we mapped in Y000593 occurs along the outer margins of the iddingsite  
330 alteration veins, and along fractures penetrating the micro-brecciated margins of the olivine  
331 crystals (Figs. 4-8). The location of the organics does not support an origin from primary magmatic  
332 inclusions in the olivines (c.f. Steele et al. 2016) because these would be concentrated in localized  
333 areas within the olivines and not around the margins of the olivine grains. The amorphous nature  
334 of the organics (Fig. 9) indicates that Y000593 has not experienced high pressures and  
335 temperatures that would produce crystalline graphitic carbon or diamonds, expected from intense  
336 impact-induced shock metamorphism (Garvie and Busek 2006, Steele et al. 2010). Nor is the  
337 Y000593 organic carbon hosted by shock-melt veins, as seen in recent studies of the martian  
338 meteorite Tissint for example (Lin et al. 2014). In addition, we exclude electrochemical reduction  
339 as a source for the organic carbon as recently proposed by Steele et al. (2018), for some of the  
340 reduced carbon found in the meteorites Tissint, Nakhla, and NWA 1950 where the carbon is  
341 intimately linked to titano-magnetite, sulfides, and their alteration products, which differs from the  
342 close association with iddingsite and olivine that we see in Y000593. Thus we propose that the  
343 organic carbon was either remobilized by, or perhaps sourced from early hydrothermal alteration  
344 processes that formed the iddingsite veins in an impact crater on Mars, and we will now explore  
345 this environment and associated alteration processes.

346

#### 347 4.3 Model for the Y000593 microalteration textures and organics

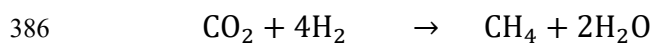
348 Indigenous organic carbon has been found in several Martian meteorites and a variety of  
349 sources have been proposed, including: (i) high-pressure impact generation (Steele et al. 2010);  
350 (ii) primary igneous i.e. magmatic processes (e.g. Steele et al. 2012); (iii) electrochemical  
351 reduction (e.g. Steele et al. 2018); (iv) dead martian organisms (McKay et al. 1996); (v) reactions  
352 in rapidly cooling magmatic and, or impact generated gases (Zolotov and Shock 2000); (vi)  
353 subsurface hydrothermal fluids (Lin et al. 2014, Steele et al. 2014); and (vii) exogenous delivery  
354 to Mars (e.g. Sephton et al. 2002;). On the basis of the distribution and ultrastructure of the organics  
355 in Y00593 (see discussion of the TEM-EELS data in the previous section) we have excluded the  
356 first three potential sources. Now, considering source (iv) for the Y000593 organics, namely that  
357 they are derived from fossilized, perhaps hyperthermophilic martian micro-organisms we find this  
358 to be unlikely. The shape and distribution of the organics that occur in sub-micron bands and sub-  
359 spherical concentrations (Fig 6-8), does not provide morphological evidence for microfossil-like  
360 objects to support a biogenic origin. In addition, given that we have rejected a biological origin for  
361 the micro-alteration textures in the Y000593 olivines, we conclude that a biotic source for the  
362 organics is unsupported by the current data.

363 Considering abiotic synthesis of the organics, there are at least two possible pathways we need  
364 to explore, either reactions in rapidly cooling impact generated gases, source (v) above; or  
365 subsurface Fischer Tropsch-type (FTT) reactions, source (vi) above. Considering first,  
366 hydrocarbon synthesis from impact generated gases, this seems very probable given the setting of  
367 Yamato 000593 and this is a mechanism that was first proposed for the PAHs (polycyclic aromatic  
368 hydrocarbons) found in the martian meteorite ALH84001 (Zolotov and Shock 2000). It has been



369 shown in experimental studies and thermodynamic calculations that impact heating events cause  
370 dissociation of ferrous carbonates in particular siderite, to yield fine grained magnetite, formation  
371 of a CO-rich local gas phase, and reduction of water vapor to form H<sub>2</sub>. Rapid cooling and high-  
372 temperature quenching of the CO-, H<sub>2</sub>-rich impact gases can lead to magnetite-catalyzed  
373 hydrocarbon synthesis (Zolotov and Shock 2000, McCollom 2003; Milesi et al. 2015). In addition,  
374 rapid cooling of trapped primary magmatic gases can generate organics (Zolotov and Shock 1999),  
375 especially if cooling was rapid enough to prevent reequilibration, and these early hydrocarbons  
376 can be aromatized by subsequent impact reheating (Zolotov and Shock 2000). Given the location  
377 of Y000593 in an impact crater and the occurrence of siderite in this meteorite, the aforementioned  
378 mechanisms for organic carbon synthesis seem probable.

379         Considering sub-surface hydrothermal processes, it has been found that the hydration of  
380 olivines and pyroxenes in serpentinizing mafic-ultramafic crust on earth and in laboratory  
381 experiments yields H<sub>2</sub> and CH<sub>4</sub> (Shock 1990; Berndt et al. 1996; McCollom and Seewald 2001,  
382 2006). The CH<sub>4</sub> is considered to be produced by Fischer–Tropsch Type (FTT) reactions involving  
383 H<sub>2</sub> and a carbon-bearing molecule principally CO, or CO<sub>2</sub> in the gas phase, or in aqueous solution,  
384 catalyzed by magnetite, following the reaction(s):



387 Short-chain hydrocarbons can also be produced by these reactions and have been identified in  
388 hydrothermal fluids discharged at mid-ocean ridge systems and in products from analog  
389 experiments (e.g. McCollom and Seewald 2001, Konn et al. 2009, Holm and Charlou 2001).  
390 Recent studies of natural serpentinites from the Mid-Atlantic Ridge (Ménez et al. 2012, 2018a)  
391 and a 90 Ma Tethyan ophiolite (Sforna et al. 2018) have documented reduced organic carbon

392 associated with the alteration minerals (fig. 2 in Sforza et al. 2018). On Mars such reactions have  
393 been suggested as important contributors to the inventory of atmospheric CH<sub>4</sub> (Oze and Sharma  
394 2005) and could also be a source of PAHs found in meteorites (Zolotov and Shock 1999). When  
395 considering the organics in Y000593 it is important to realise however, that the synthesis of  
396 organics by FT-type reactions is very slow at lower temperatures (McCollom and Donaldson,  
397 2015) like those estimated by Bridges and Schwenzer (2012) for the Yamato hydrothermal system.  
398 Moreover, it is now becoming apparent that whilst serpentinization reactions yield abundant H<sub>2</sub> the  
399 formation of methane and other hydrocarbons is kinetically inhibited during circulation of  
400 seawater through serpentinite-hosted hydrothermal systems, and that these compounds may be  
401 derived from elsewhere in the terrestrial system (e.g., McDermott et al. 2015; Wang et al., 2018;  
402 McCollom, 2016). In short it seems unlikely that FT-type processes may have synthesized significant  
403 amounts of organics in the Yamato impact crater, and that hydrothermal circulation may rather  
404 have been important for re-distributing organics derived from other abiotic sources.

405 Comparing the Carbon XANES (X-ray absorption near edge spectroscopy) measured on  
406 organic carbon found in terrestrial seafloor serpentinizing systems (e.g. figure 6 Ménez et al.  
407 2018b) to our TEM-EELS data, reveals important spectral differences. For example, Ménez et al.  
408 (2018b) report C-K edge spectra with a well-defined peak at 288.6 eV attributed to carboxyl  
409 functional group, in contrast to our EELS spectra (Fig. 9b) that show two peaks, described in the  
410 results section above, and interpreted to reflect significant amounts of C=C bonding most likely in  
411 polyaromatic domains that lack long range order (Garvie and Busek 2006). The much higher  
412 aromatic carbon content of our organics from Yamato, is difficult to explain by purely FT-type  
413 processes, especially at the temperatures <200°C. Alternative sources for the organics in Y000593  
414 may therefore be more consistent with our EELS spectra, involving abiotic processes in rapidly

415 cooling impact gases as discussed above (source v), and/or hydrothermal re-heating of  
416 magmatically derived organic carbon that can cause aromatization.

417 A further potential source for the Y000593 organics is from the exogenous delivery of organics  
418 to the martian surface. Many organic molecules are known to be produced abiotically by  
419 astrochemistry in the interstellar medium and circumstellar regions (Herbst and van Dishoeck  
420 2009), and become incorporated in the planet-forming disks of new star systems (Shaw 2007).  
421 Extraterrestrial delivery of such organics aboard (micro)meteorites, asteroids, and comets to Mars  
422 could be a significant contributor to the planets organic inventory (Pierazzo and Chyba 1999). It  
423 is therefore plausible that the organic carbon found in the iddingsite veins of Yamato 000593 was  
424 derived from exogenous organics condensed onto the Martian surface that were later redistributed  
425 into the subsurface by hydrothermal fluids circulating in the impact crater. It is also possible that  
426 the impacting bollide itself may have delivered the organics, particularly if it was a carbonaceous  
427 chondrite, or organic rich comet (Ehrenfreund and Charnley 2000). Such a scenario involving  
428 extra-Martian delivery of organics cannot be excluded on the basis of our data for the origin of the  
429 carbon we mapped in Y000593.

430 To summarise the microtextural history and potential sources for organic carbon in Yamato  
431 00593 we have compiled a schematic diagram showing the sequence of events (Figure 10). There  
432 are three main stages: T1 shows the Nakhla family of meteorites located in the near subsurface of  
433 Mars, their magmatic crystallization age being  $1310 \pm 30$  Ma (Borg and Drake 2005) with possible  
434 condensation of exogenous organics onto the Martian surface; T2 shows fracturing of the Martian  
435 crust due to an impact event that caused micro-brecciation of the Yamato olivines, with possible  
436 delivery of organics aboard the impacting bolloid, and or synthesis of organics from high-  
437 temperature impact gases, with melting of the permafrost leading to hydrothermal circulation; T3

438 shows subsurface hydrothermal circulation with aqueous alteration of the Martian crust and  
439 iddingsite formation at c. 633Ma (Borg and Drake 2005), re-distribution of organics into the  
440 subsurface carried by the hydrothermal fluids and possible, minor organic carbon synthesis by FT-  
441 type processes. These events were followed by a much later second impact event at c. 11 Ma that  
442 was responsible for ejection of the Nakhla family of meteorites from Mars (Imae et al. 2003) and  
443 delivery to Earth.

444

## 445 **5. Implications for seeking biosignatures in ultramafic rocks and impact structures on Earth** 446 **and Mars**

447 In this study, we present abiotic mechanisms of generating both organic carbon and complex  
448 microalteration textures in altered olivines of the martian meteorite Y000593 that have  
449 implications for seeking textural and chemical biosignatures in ultramafic rocks on Earth. The  
450 Yamato microtextures were previously compared by White et al. (2014) to candidate biosignatures  
451 found in altered volcanic glasses, however, there is now a maturing body of work that has  
452 questioned the role of microbes in the formation of terrestrial “bioalteration” textures. Many early  
453 workers favoured a microbial origin for so called bioalteration textures found in seafloor glasses  
454 (e.g. Thorseth et al. 1992; Fisk 1998; Banerjee et al. 2003; Staudigel et al. 2008), but an increasing  
455 number of petrological and experimental studies have questioned the contribution of microbes to  
456 seafloor volcanic glass dissolution and suggested a range of possible abiotic mechanisms (e.g. Alt  
457 and Mata 2000; Knowles et al. 2012; Fisk et al. 2013; French and Blake 2016; Fisk et al. 2019),  
458 particularly for the granular microalteration textures (McCollom and Donaldson 2019), and also  
459 for microtextures found in ancient meta-volcanic glasses (Grosch and McLoughlin, 2014; Lepot  
460 et al. 2011). This study expands the range of known abiotic alteration processes recorded by olivine

461 microalteration textures, and reports high-magnification imaging and chemical mapping data not  
462 yet reported from similar olivine microalteration textures found in terrestrial ultramafic rocks (Fisk  
463 et al. 2006).

464 We note that optical and SEM images of the Yamato microtextures (Fig 1-3 herein, also  
465 White et al. 2014) closely resemble features previously reported from olivines in the Nakhla  
466 meteorite, with apparently linear reddish-brown microtextures propagating at high angles to the  
467 iddingsite veins into the olivine crystals (see fig. 3c in Fisk et al. 2006, fig. 1c in Lee et al. 2015,  
468 and Gibson et al. 2006). We postulate that when these microtextures in the Nakhla meteorite are  
469 imaged using similar techniques to those employed here that a complex micro-brecciated interface  
470 between the olivine and iddingsite alteration may also be revealed. We suggest that previous lower-  
471 magnification imaging of the Y000593 olivine crystal margins may have given the appearance of  
472 apparent linear microtextures at high angles to the iddingsite veins, which were then compared to  
473 terrestrial bioalteration tunnels, but that when these are imaged at higher magnification and in 3-  
474 dimensions then their more complex morphology becomes apparent.

475 In this study, we argue that impact induced brecciation and fracturing in a martian impact crater  
476 is responsible for the microtextures found in olivines of Y000593, and this leads us to consider the  
477 prevalence of such processes in terrestrial impact sites. For example, in a previous discussion  
478 concerning enigmatic tubular microtextures found in impact glasses of the 14.6 Ma Reis impact  
479 structure, which were compared to terrestrial bioalteration textures of argued microbial origin by  
480 Sapers et al. (2014, 2014a, 2015), it was suggested that shock related processes needed to be more  
481 fully explored as an alternative origin for these microtextures and associated organics  
482 (McLoughlin and Grosch 2014, Sapers et al. 2014a). This current study reasserts that shock related  
483 processes can generate complex microalteration textures in impact rocks, albeit on Mars rather

484 than Earth, and that there are a range of abiotic processes for generating and redistributing organics  
485 within rocks of the impact site. Taken together, our findings caution that although post-impact  
486 hydrothermal systems on Earth and Mars may be potential locations for the origins and emergence  
487 of life (e.g. Cockell 2006; Grosch et al. 2014), alteration textures and organics associated with  
488 iddingsite alteration are not necessarily biosignatures in these environments.

489

490 **References:**

491 Alt, J.C. and Mata, P., (2000) On the role of microbes in the alteration of submarine basaltic glass:  
492 a TEM study. *Earth and Planetary Science Letters* 181: 301–313.

493 Banerjee, N. R., & Muehlenbachs, K. (2003). Tuff life: Bioalteration in volcanoclastic rocks from  
494 the Ontong Java Plateau. *Geochemistry, Geophysics, Geosystems*, 4(4).

495 Bernard, S., Beyssac, O., Benzerara, K., Findling, N., Tzvetkov, G., & Brown Jr, G. E. (2010).  
496 XANES, Raman and XRD study of anthracene-based cokes and saccharose-based chars  
497 submitted to high-temperature pyrolysis. *Carbon*, 48(9), 2506-2516.

498 Berndt, M. E., Allen, D. E., & Seyfried Jr, W. E. (1996). Reduction of CO<sub>2</sub> during serpentinization  
499 of olivine at 300 C and 500 bar. *Geology*, 24(4), 351-354.

500 Bishop, J.L., Dobrea, E.Z.N., McKeown, N.K., Parente, M., Ehlmann, B.L., Michalski, J.R.,  
501 Milliken, R.E., Poulet, F., Swayze, G.A., Mustard, J.F. and Murchie, S.L., (2008).  
502 Phyllosilicate diversity and past aqueous activity revealed at Mawrth Vallis, Mars. *Science*:  
503 321(5890), 830-833.

504 Borg, L. & Drake, M.J. (2005). A review of meteorite evidence for the timing of magmatism and  
505 of surface or near-surface liquid water on Mars. *J. Geophys. Res.*: 110, E12S03.

506 Bridges, J.C., & Schwenzer, S.P. (2012). The nakhlite hydrothermal brine on Mars. *EPSL*: 359–  
507 360, 117–123.

508 Changela, H.G. & Bridges, J.C. (2011). Alteration assemblages in the nakhlites: variation with  
509 depth on Mars. *Meteorit. Planet. Sci.* 45: 1847–1867.

510 Chatzitheodoridis, E., Haigh, S. and Lyon, I., (2014). A conspicuous clay ovoid in Nakhla:  
511 evidence for subsurface hydrothermal alteration on Mars with implications for astrobiology.  
512 *Astrobiology*: 14(8), 651-693.

513 Cockell, C.S. (2006) The origin and emergence of life under impact bombardment. *Philos Trans*  
514 *R Soc Lond B Biol Sci* 361:1845–1856.

515 Cody, G.D., Yabuta, H., Kilcoyne, A.L.D., Araki, T., Ade, H., Dera, P., Fogel, M., Militzer, B.  
516 and Mysen, B.O. (2008). Organic thermometry for chondritic parent bodies. *Earth and*  
517 *Planetary Science Letters*, 272: 446-455.

518 Ehlmann, B. L., Mustard, J. F., Murchie, S. L., Bibring, J. P., Meunier, A., Fraeman, A. A., &  
519 Langevin, Y. (2011). Subsurface water and clay mineral formation during the early history of  
520 Mars. *Nature*, 479(7371), 53.

521 Ehrenfreund P. and Charnley S. (2000). Organic molecules in the interstellar medium, comets, and  
522 meteorites: A voyage from dark clouds to the Early Earth. *Annual Review of Astronomy and*  
523 *Astrophysics* 38:427–483.

524 Eugster, O., *et al.* (2002). Ejection ages from krypton-81-krypton-83 dating and pre-atmospheric  
525 sizes of martian meteorites. *Meteorit. Planet. Sci.* 37, 1345–1360.

526 Fisk, M.R., Popa, R., Mason, O.U., Storrie-Lombardi, M.C. and Vicenzi, E.P., (2006). Iron-  
527 magnesium silicate bioweathering on Earth (and Mars?). *Astrobiology*: 6(1), 48-68.

528 Fisk, M. R., Giovannoni, S. J., & Thorseth, I. H. (1998). Alteration of oceanic volcanic glass:  
529 textural evidence of microbial activity. *Science*, 281(5379), 978-980.

530 Fisk, M.R. and Giovannoni, S.J. (1999) Sources of nutrients and energy for a deep biosphere on  
531 Mars. *J Geophys Res* 104: 11805–11815.

532 Fisk, M. R., Crovisier, J. L., & Honnorez, J. (2013). Experimental abiotic alteration of igneous and  
533 manufactured glasses. *Comptes Rendus Geoscience*, 345(4), 176-184.

534 Fisk, M.R. and McLoughlin, N. (2013). Atlas of alteration textures in volcanic glass from the  
535 ocean basins. *Geosphere* 9 (2), 317-341.

536 Fisk, M. R., Popa, R., & Wacey, D. (2019). Tunnel Formation in Basalt Glass. *Astrobiology*, 19(1),  
537 132-144.

538 French, J. E., & Blake, D. F. (2016). Discovery of naturally etched fission tracks and alpha-recoil  
539 tracks in submarine glasses: reevaluation of a putative biosignature for Earth and Mars.  
540 *International Journal of Geophysics*, 2016.

541 Furnes H, Staudigel H, Thorseth IH, Torsvik T, Muehlenbachs K, Tumyr O (2001) Bioalteration  
542 of basaltic glass in the oceanic crust. *Geochem Geophys Geosyst* 2(8):  
543 doi:10.129/2000GC000150



544 Garvie, L.A.J., & Busek, P.R. (2006). Carbonaceous materials in the acid residue from the Orgueil  
545 carbonaceous chondrite meteorite. *Meteoritics & Planetary Science*: 41, 633–642.

546 Gibson et al. (2006). Observation and analysis of in situ carbonaceous matter in Nakhla: part II.  
547 LPSC XXXVII abstract #2039.

548 Gooding, J. L., Wentworth, S. J., & Zolensky, M. E. (1991). Aqueous alteration of the Nakhla  
549 meteorite. *Meteoritics*, 26(2), 135-143.

550 Grosch, E.G., McLoughlin, N., Lanari, P., Erambert, M. and Vidal, O., (2014). Microscale  
551 mapping of alteration conditions and potential biosignatures in basaltic-ultramafic rocks on  
552 early Earth and beyond. *Astrobiology*: 14(3), 216-228.

553 Grosch, E.G. and Mcloughlin, N. (2014) Reassessing the biogenicity of Earth's oldest trace fossil  
554 with implications for biosignatures in the search for early life. *Proceedings of the National*  
555 *Academy of Sciences* 111: 8380-8385

556 Herbst E. and Van Dishoeck E. (2009). Complex organic interstellar molecules. *Annual Review*  
557 *of Astronomy and Astrophysics* 47:427–480.

558 Holm N.G. Charlou J.L., (2001). Initial indications of abiotic formation of hydrocarbons in the  
559 Rainbow ultramafic hydrothermal system, Mid-Atlantic Ridge: *Earth and Planetary Science*  
560 *Letters*, 191, 1–8.

561 Imae, N., Ikeda, Y., Shinoda, K., Kojima, H. and Iwata, N., (2003). Yamato nahklites: Petrography  
562 and mineralogy. *Antarctic Meteorite Research*: 16, 13-33.

563 Kelley D.S., Karson, J.A., Früh-Green, G.L., Yoerger, D.R., Shank, T.M., Butterfield, D.A.,  
564 Hayes, J.M., Schrenk, M.O., Olson, E.J., Proskurowski, G. and Jakuba, M.,(2005). A  
565 serpentinite-hosted ecosystem: The lost city hydrothermal field. *Science*: 307, 1428–1434.

566 Knowles, E., Wirth, R., and Templeton, A. (2012) A Comparative analysis of potential  
567 biosignatures in basalt glass by FIB-TEM. *Chemical Geology* 330-331: 165-175.

568 Konn, C., Charlou, J. L., Donval, J. P., Holm, N. G., Dehairs, F., & Bouillon, S. (2009).  
569 Hydrocarbons and oxidized organic compounds in hydrothermal fluids from Rainbow and Lost  
570 City ultramafic-hosted vents. *Chemical Geology*, 258(3-4), 299-314.

571 Lee, M.R., MacLaren, I., Andersson, S.M.L., Kovacs, A., Tomkinson, T., Mark, D.F. and Smith,  
572 C.L., (2015). Opal-A in the Nakhla meteorite: A tracer of ephemeral liquid water in the  
573 Amazonian crust of Mars. *Meteoritics & planetary science*: 50(8), 1362-1377.

574 Lepot, K., Benzerara, K., & Philippot, P. (2011). Biogenic versus metamorphic origins of diverse  
575 microtubes in 2.7 Gyr old volcanic ashes: Multi-scale investigations. *Earth and Planetary  
576 Science Letters*, 312(1-2), 37-47.

577 Lin, Y., El Goresy, A., Hu, S., Zhang, J., Gillet, P., Xu, Y., Hao, J., Miyahara, M., Ouyang, Z.,  
578 Ohtani, E. and Xu, L., (2014). NanoSIMS analysis of organic carbon from the Tissint Martian  
579 meteorite: Evidence for the past existence of subsurface organic-bearing fluids on Mars.  
580 *Meteoritics & Planetary Science*: 49(12), 2201-2218.

581 McCollom, T. M. (2016). Abiotic methane formation during experimental serpentinization of  
582 olivine. *Proceedings of the National Academy of Sciences*, 119: 13965–13970.

583 McCollom, T. M. (2003). Formation of meteorite hydrocarbons from thermal decomposition of  
584 siderite (FeCO<sub>3</sub>). *Geochimica et Cosmochimica Acta*, 67, 311–317.

585 McCollom, T. M., & Seewald, J. S. (2001). A reassessment of the potential for reduction of  
586 dissolved CO<sub>2</sub> to hydrocarbons during serpentinization of olivine. *Geochimica et*  
587 *Cosmochimica Acta*, 65(21), 3769-3778.

588 McCollom, T. M., & Seewald, J. S. (2006). Carbon isotope composition of organic compounds  
589 produced by abiotic synthesis under hydrothermal conditions. *Earth and Planetary Science*  
590 *Letters*, 243(1-2), 74-84.

591 McCollom T.M. & Seewald J.S. (2007). Abiotic synthesis of organic compounds in deep-sea  
592 hydrothermal environments. *Chemical Reviews*: 107, 382–401.

593 McCollom, T. M., & Donaldson, C. (2016). Generation of hydrogen and methane during  
594 experimental low-temperature reaction of ultramafic rocks with water. *Astrobiology*, 16(6),  
595 389-406. McCollom, T. M., & Donaldson, C. (2019). Experimental Constraints on Abiotic  
596 Formation of Tubules and Other Proposed Biological Structures in Subsurface Volcanic Glass.  
597 *Astrobiology*, 19(1), 53-63.

598 McDermott, J. M., Seewald, J. S., German, C. R., & Sylva, S. P. (2015). Pathways for abiotic  
599 organic synthesis at submarine hydrothermal fields. *Proceedings of the National Academy of*  
600 *Sciences*, 112(25), 7668-7672.

601 McKay, D.S., Gibson Jr, E.K., Thomas-Keprta, K.L. and Vali, H., (1996). Search for past life on  
602 Mars: possible relic biogenic activity in Martian meteorite ALH84001. *Science*: 273(5277),  
603 924.

604 McLoughlin, N. & Grosch, E. (2015). A Hierarchical System for Evaluating the Biogenicity of  
605 Metavolcanic- and Ultramafic-Hosted Microalteration Textures in the Search for  
606 Extraterrestrial Life. *Astrobiology* 15: DOI: 10.1089/ast.2014.1259.

607 McLoughlin, N. and Grosch, E.G. (2014). Enigmatic tubular features in impact glass:  
608 COMMENT. *Geology*, 42, e346-e346.

609 McLoughlin, N., Wacey, D., Kruber, C., Kilburn, M.R., Thorseth, I.H. and Pedersen, R.B., (2011).  
610 A combined TEM and NanoSIMS study of endolithic microfossils in altered seafloor basalt.  
611 *Chemical Geology*, 289, 54-162.

612 Ménez, B., Pasini, V., and Brunelli, D. (2012) Life in the hydrated suboceanic mantle. *Nature*  
613 *Geoscience* 5:133–137.

614 Ménez, B., Pisapia, C., Andreani, M., Jamme, F., Vanbellingen, Q.P., Brunelle, A., Richard, L.,  
615 Dumas, P. and Réfrégiers, M., (2018a). Abiotic synthesis of amino acids in the recesses of the  
616 oceanic lithosphere. *Nature*, 564: 59

617 Ménez, B., Pasini, V., Guyot, F., Benzerara, K., Bernard, S., & Brunelli, D. (2018b).  
618 Mineralizations and transition metal mobility driven by organic carbon during low-temperature  
619 serpentinization. *Lithos*, 323, 262-276. Michalski, J.R., Cuadros, J., Niles, P.B., Parnell, J.,  
620 Rogers, A.D. and Wright, S.P., (2013). Groundwater activity on Mars and implications for a  
621 deep biosphere. *Nature Geoscience*: 6(2), 133-138.

622 Mikouchi, T., Koizumi, E., Monkawa, A., Ueda, Y. and Miyamoto, M., (2003). Mineralogy and  
623 petrology of Yamato 000593: Comparison with other Martian nakhlite meteorites. *Antarctic*  
624 *Meteorite Research*: 16, 34-57.

625 Milesi, V., Guyot, F., Brunet, F., Richard, L., Recham, N., Benedetti, M., Dairou, J., & Prinzhofer,  
626 A. (2015). Formation of CO<sub>2</sub>, H<sub>2</sub> and condensed carbon from siderite dissolution in the 200–  
627 300°C range and at 50 MPa. *Geochimica et Cosmochimica Acta*, 154: 201-211.

628 Ming, D.W., Archer, P.D., Glavin, D.P., Eigenbrode, J.L., Franz, H.B., Sutter, B., Brunner, A.E.,  
629 Stern, J.C., Freissinet, C., McAdam, A.C. and Mahaffy, P.R., (2014). Volatile and organic  
630 compositions of sedimentary rocks in Yellowknife Bay, Gale Crater, Mars. *Science*:  
631 343(6169), 1245267.

632 Muntener, O. (2010). Serpentine and serpentinization: A link between planet formation and life.  
633 *Geology* (2010) 38 (10): 959-960.

634 Mustard, J. F., Murchie, S. L., Pelkey, S. M., Ehlmann, B. L., Milliken, R. E., Grant, J. A., ... &  
635 Roach, L. (2008). Hydrated silicate minerals on Mars observed by the Mars Reconnaissance  
636 Orbiter CRISM instrument. *Nature*, 454(7202), 305.

637 Nyquist, L. E., Bogard, D. D., Shih, C. Y., Greshake, A., Stöffler, D., & Eugster, O. (2001). Ages  
638 and geologic histories of Martian meteorites. In *Chronology and evolution of Mars* (pp. 105-  
639 164). Springer, Dordrecht.

640 Oze, C., & Sharma, M. (2005). Have olivine, will gas: serpentinization and the abiogenic  
641 production of methane on Mars. *Geophysical Research Letters*, 32(10).

642 Pierazzo E. and Chyba C. F. (1999). Amino acid survival in large cometary impacts. *Meteoritics*  
643 & *Planetary Science* 34:909–918.

644 Russell M.J., (2007). The alkaline solution to the emergence of life: energy, entropy and early  
645 evolution: *Acta Biotheoretica*, 55, 133–179.

646 Sapers, H. M., Osinski, G. R., Banerjee, N. R., & Preston, L. J. (2014). Enigmatic tubular features  
647 in impact glass. *Geology*, 42(6), 471-474.

648 Sapers, H. M., Banerjee, N. R., Osinski, G. R., Preston, L. J., & Ferrière, L. (2014a). Enigmatic  
649 tubular features in impact glass: REPLY. *Geology*, 42(9), e348-e348.

650 Sapers, H. M., Banerjee, N. R., & Osinski, G. R. (2015). Potential for impact glass to preserve  
651 microbial metabolism. *Earth and Planetary Science Letters*, 430, 95-104.

652 Schulte, M., Blake, D., Hoehler, T., & McCollom, T. (2006). Serpentinization and its implications  
653 for life on the early Earth and Mars. *Astrobiology*, 6(2), 364-376.

654 Sephton, M.A. *et al.* (2002). High molecular weight organic matter in martian meteorites.  
655 *Planetary and Space Science* 50: 711-716.

656 Sforza, M. C., Brunelli, D., Pisapia, C., Pasini, V., Malferrari, D., & Ménez, B. (2018). Abiotic  
657 formation of condensed carbonaceous matter in the hydrating oceanic crust. *Nature*  
658 *communications*, 9(1), 5049.

659 Shaw A. M., 2007. *Astrochemistry: From astronomy to astrobiology*. England: Wiley, pp

660 Shih C.Y., Wiesmann, H., Nyquist, H., and Misawa, K. (2002) Crystallization age of Antarctic  
661 Nakhlite Y000593: Further evidence of Nakhlite launch pairing (abs). *Antarctic Meteorites*  
662 XXVII, 151-153, *Nat. Inst. Polar Res., Tokyo*.

663 Shock, E. L. (1990). Geochemical constraints on the origin of organic compounds in hydrothermal  
664 systems. *Origins of Life and Evolution of the Biosphere*, 20(3-4), 331-367.

665 Squyres, S.W., Arvidson, R.E., Bell, J.F., Calef, F., Clark, B.C., Cohen, B.A., Crumpler, L.A., De  
666 Souza, P.A., Farrand, W.H., Gellert, R. and Grant, J., (2012). Ancient impact and aqueous  
667 processes at Endeavour Crater, Mars. *Science*: 336(6081), 570-576.

668 Staudigel, H., Furnes, H., McLoughlin, N., Banerjee, N. R., Connell, L. B., & Templeton, A.  
669 (2008). 3.5 billion years of glass bioalteration: Volcanic rocks as a basis for microbial life?  
670 *Earth-Science Reviews*, 89(3-4), 156-176.

671 Steele, A., Benning, L.G., Wirth, R., Siljeström, S., Fries, M.D., Hauri, E., Conrad, P.G., Rogers,  
672 K., Eigenbrode, J., Schreiber, A. and Needham, A., (2018). Organic synthesis on Mars by  
673 electrochemical reduction of CO<sub>2</sub>. *Science advances*, 4: p.eaat51118.

674 Steele, A., McCubbin, F.M., Fries, M.D. (2016). The provenance, formation, and implications of  
675 reduced carbon phases in Martian meteorites. *Meteoritics & Planetary Science* 51: 1–23.

676 Steele, A., McCubbin, F.M., Benning, L.G., Siljestroem, S., Cody, G.D., Goreva, Y., Hauri, E.H.,  
677 Wang, J., Kilcoyne, A.L.D., Grady, M. and Verchovsky, A., (2014). Hydrothermal organic  
678 synthesis on Mars: Evidence from the Tissint meteorite. In *Meteoritics & Planetary Science*:  
679 49, A376-A376.

680 Steele, A., McCubbin, F.M., Fries, M.D., Golden, D.C., Ming, D.W. and Benning, L.G., (2012).  
681 Graphite in the martian meteorite Allan Hills 84001. *American Mineralogist*: 97(7), 1256-  
682 1259.

683 Steele, A., McCubbin, F.M., Fries, M., Kater, L., Boctor, N.Z., Fogel, M.L., Conrad, P.G.,  
684 Glamoclija, M., Spencer, M., Morrow, A.L. and Hammond, M.R., (2012). A reduced organic  
685 carbon component in martian basalts. *Science*: 337(6091), 212-215.

686 Steele, A., McCubbin, F.M., Fries, M., Glamoclija, M., Kater, L. and Nekvasil, H., (2010).  
687 Graphite in an Apollo 17 impact melt breccia. *Science*: 329(5987), 51-51.

688 Thorseth, I. H., Furnes, H., & Heldal, M. (1992). The importance of microbiological activity in  
689 the alteration of natural basaltic glass. *Geochimica et Cosmochimica Acta*, 56(2), 845-850.

690 Treiman, H. A. (2005). The Nakhrites: Augite-rich igneous rocks from Mars. *Chemie De Erder*  
691 65: 203-270.

692 Treiman, H. A., & Goodrich, A. C. (2002). Pre-terrestrial aqueous alteration of the Y000749  
693 nakhlite meteorite. In *Antarctic Meteorites XXVII* (Vol. 27, pp. 166-167).

694 Türke, A., Nakamura, K., & Bach, W. (2015). Palagonitization of basalt glass in the flanks of mid-  
695 ocean ridges: implications for the bioenergetics of oceanic intracrustal ecosystems.  
696 *Astrobiology*, 15(10), 793-803.

697 Velbel, M. A. (2016). Aqueous corrosion of olivine in the Mars meteorite Miller Range (MIL)  
698 03346 during Antarctic weathering: Implications for water on Mars. *Geochimica et*  
699 *Cosmochimica Acta*, 180, 126-145.

700 Velbel, M. A. (2009). Dissolution of olivine during natural weathering. *Geochimica et*  
701 *Cosmochimica Acta*, 73(20), 6098-6113.



702 Wang, D. T., Reeves, E. P., McDermott, J. M., Seewald, J. S., & Ono, S. (2018). Clumped  
703 isotopologue constraints on the origin of methane at seafloor hot springs. *Geochimica et*  
704 *Cosmochimica Acta*, 223, 141-158.

705 White, L.M., Gibson, E.K., Thomas-Keprta, K.L., Clemett, S.J. and McKay, D.S., (2014). Putative  
706 indigenous carbon-bearing alteration features in martian meteorite Yamato 000593.  
707 *Astrobiology*: 14(2), 170-181.

708 Zolotov, M., & Shock, E. (1999). Abiotic synthesis of polycyclic aromatic hydrocarbons on Mars.  
709 *Journal of Geophysical Research: Planets*, 104(E6), 14033-14049.

710 Zolotov, M. Y., & Shock, E. L. (2000). An abiotic origin for hydrocarbons in the Allan Hills 84001  
711 martian meteorite through cooling of magmatic and impact-generated gases. *Meteoritics &*  
712 *Planetary Science*, 35(3), 629-638.

713

714 **Figure Captions:**

715

716 **Fig. 1.** Morphology of alteration textures in olivine crystals of Martian meteorite Y000593. **(a)**  
717 Optical image of reddish brown iddingsite alteration along curving cracks in olivine (ol). **(b)**  
718 Iddingsite filled fractures on the margins of an olivine grain (arrowed). **(c)** Higher magnification  
719 image showing apparently linear features (arrowed) on the margins of the iddingsite filled fractures  
720 in an olivine grain. **(d)** BSE (back scatter electron) image of an olivine crystal containing fractures  
721 filled with banded iddingsite that shows a central band of more compact iddingsite (white arrows)  
722 and outer poorly crystalline iddingsite that shows a complex interface with the margins of the  
723 olivine crystal (black arrows). **(e)** Enlarged image showing the progressive alteration of an olivine

724 crystal (top left) to iddingsite (lower right). **(f)** HAADF STEM (high angle annular dark field  
725 scanning transmission electron microscopy) image of a FIB lamella cut across an iddingsite filled  
726 fracture showing the highly brecciated margin of the olivine (Ol) crystal and banded nature of the  
727 iddingsite. **(g)** Bright field TEM image showing angular brecciated margin of an olivine crystal.  
728 Complex contrast variations within the olivine are evidence of the highly defective and strained  
729 crystal. **(h)** Bright field TEM image showing angular fragments of olivine (Ol) with amorphous  
730 iddingsite alteration filling the fractures in between. Scale bar is 50  $\mu\text{m}$  in (a and b), 10  $\mu\text{m}$  in (c),  
731 and 2  $\mu\text{m}$  in (d-f), 0.5  $\mu\text{m}$  in (g-h).

732

733 **Fig. 2.** SEM-EDS maps of a fractured olivine grain (Ol) adjacent to a pyroxene grain (pyx). The  
734 fractures are filled with banded alteration products, collectively termed iddingsite that show a  
735 ramified interface with the host olivine. The  $K\alpha$  peak of the elements Si, Mg, Fe, O and Al were  
736 measured. The maps show a central fracture-filling alteration phase (iddingsite 1) that is relatively  
737 enriched in Si (black arrow), and an outer alteration phase (iddingsite 2) that is more enriched in  
738 Fe and O (white arrow). Note the dark area at the interface between the olivine and pyroxene grains  
739 is void space. Also the iddingsite in the lower fracture can be seen to have contracted and pulled  
740 away from the margin of the fracture. Scale bar is 5  $\mu\text{m}$ , the intensity of the colour scale reflects  
741 the relative concentration of the individual elements.

742

743 **Fig. 3.** SEM images showing the location of the FIB lamellas cut from Y000593 and studied by  
744 TEM, plus examples of selected area electron diffraction patterns from olivine and alteration  
745 phases within Y000593. **(a)** FIB lamella 1 cut parallel to the margins of the iddingsite filled vein  
746 intersecting the ramified interface with the olivine (Ol) crystal, for TEM data see Fig. 8 **(b)** FIB

747 lamella 3 cut oblique to a vein in the olivine filled with banded iddingsite, for TEM data see Fig.  
748 6; (c) FIB lamella 2 cut orthogonal to an iddingsite filled vein in the olivine; (d) the same FIB  
749 lamella mounted on a Cu TEM grid during thinning to reveal the “saw tooth” interface (arrowed)  
750 between the olivine and alteration products seen beneath the sample surface. (e) Diffraction pattern  
751 from a single olivine crystal with the beam parallel to the [001] axis, showing lattice parameters  
752 of  $a=4.84 \text{ \AA}$  and  $b=10.38 \text{ \AA}$ . (f) Diffraction pattern from another single olivine crystal with the  
753 beam parallel to [100], showing the lattice parameter of  $c=6.08 \text{ \AA}$ . Note that these are very close  
754 to the lattice parameters of the fayalite end member of the olivine solid solution series ( $a= 4.82 \text{ \AA}$ ;  
755  $b= 10.47 \text{ \AA}$ ;  $c=6.10 \text{ \AA}$ ). (g) Diffraction pattern from the iddingsite 1 phase, showing distinct ring  
756 patterns with d-spacings of c.  $2.59 \text{ \AA}$  and  $4.40 \text{ \AA}$ , consistent with the (131) and (111) planes of  
757 nontronite, a smectitic clay. (h) Diffraction pattern from the iddingsite 2 phase. In addition to ring  
758 patterns, it possesses elongated spots with d-spacings of c.  $1.43 \text{ \AA}$ ,  $2.26 \text{ \AA}$  and  $2.43 \text{ \AA}$ , consistent  
759 with the (121), (211) and (111) planes of goethite. Scale bars are  $5 \mu\text{m}$ .

760

761 **Fig. 4.** Chemistry of iddingsite alteration in fractured olivine (grain 4, area 1) of martian meteorite  
762 Y000593 characterized by NanoSIMS ion mapping of the boxed area (yellow) in the left hand  
763 BSE (back scatter electron) image. The brecciated morphology of the olivine crystal margins is  
764 clearly seen in the  $S^-$  map for example. Organic material (measured as  $CN^-/C^-$  to exclude any  
765 possible contamination from resin) occurs as bands along the margins of the iddingsite filled  
766 fracture and extends into the brecciated margins of the altered olivine. Intensity calibration bars  
767 are expressed as total counts for  $FeO^-$ ,  $O^-$  and  $S^-$ , and as a simple ratio for  $CN^-/C^-$ .

768

769 **Fig. 5.** Chemistry of iddingsite alteration in fractured olivine (grain 5, area 2) of martian meteorite  
770 Y000593 characterized by NanoSIMS ion mapping of the boxed area (yellow) in the left hand  
771 BSE (back scatter electron) image. The brecciated morphology of the olivine crystal margins is  
772 especially clear in the S<sup>-</sup> map. Organic material (measured as CN<sup>-</sup>/C<sup>-</sup> to exclude any possible  
773 contamination from resin) occurs as a band along the margin of the iddingsite filled fracture and  
774 extends someway into the brecciated margins of the altered olivine. Intensity calibration bars are  
775 expressed as total counts for FeO<sup>-</sup>, O<sup>-</sup> and S<sup>-</sup>, and as a simple ratio for CN<sup>-</sup>/C<sup>-</sup>.

776

777 **Fig. 6.** Distribution and elemental mapping of olivine (Ol), iddingsite alteration and organic carbon  
778 in Y000593. **(a)** BF (bright field) STEM image of FIB lamella-3 (for location in sample see Fig.  
779 3b) the black boxes correspond to areas that were selected for element mapping. **(b)** High angle  
780 annular dark field (HAADF) STEM image of Area a, contains fractured olivine (lower right)  
781 adjacent to iddingsite (upper left), element maps shown beneath. **(c)** HAADF STEM image of Area  
782 b on the margin of a brecciated and altered olivine crystal (lower right), elemental maps shown in  
783 Fig. 7. **Area a** shows a pronounced band of carbon along the margins of the olivine crystal near  
784 the boundary with the iddingsite, also in the fractures that brecciate the olivine crystal margin.  
785 Crucially the C (red) and Cl (green) maps do not correlate, excluding epoxy as a source for the  
786 organic carbon. Element maps were measured using the EDS detector except for the carbon map  
787 which is a K-edge EELS map. Red boxes in b and c correspond to locations where Carbon EELS  
788 spectra were measured, see Fig. 9. Scale bars is 2µm in (a) and 1 µm in (b and c and the elemental  
789 maps).

790

791 **Fig. 7** Distribution and elemental mapping of olivine, iddingsite alteration and organic carbon in  
792 Y000593 corresponding to Area b in FIB lamellae 3 from previous Fig. 6. Area b contains a band  
793 of carbon in the upper part of the image at the boundary of iddingsite phases 1 and 2, also ovoid  
794 bodies of carbon <300 nm across in the lower right close to the olivine crystal margin. Note that  
795 the C and Cl maps do not correlate, excluding epoxy as a source for the organic carbon. Element  
796 maps were measured using the EDS detector except for the carbon map which is a K-edge EELS  
797 map. Scale bar 1  $\mu\text{m}$ , the brightness/intensity of the colour scale of the elemental maps reflects  
798 relative concentrations.

799

800 **Fig. 8** Distribution and elemental mapping of olivine, iddingsite alteration and organic carbon in  
801 Y000593 corresponding to FIB lamellae 1 mapped region 3 (for location in sample see Fig. 3a).  
802 **(a)** overview showing brecciated and highly fractured olivine in the top centre, with iddingsite  
803 alteration phases 1 and 2, and olivine grain in the lower part of the image, boxed area is enlarged  
804 in **(b)**, a small over-thinned region forming a hole in the FIB lamellae is arrowed. **(b)** HAADF  
805 image showing the fractured olivine grain with region selected for element mapping shown by the  
806 white dashed box. The Carbon EELS map shows the concentration of organic material near the  
807 margin of the olivine, and note again that the C and Cl maps do not correlate, excluding epoxy as  
808 a source for the organic carbon. Element maps were measured using the EDS detector except for  
809 the carbon map which is a K-edge EELS map. Scale bar is 2 $\mu\text{m}$  in **(a)** and 0.5  $\mu\text{m}$  in **(b)**, the  
810 brightness/intensity of the colour scale of the elemental maps reflects relative concentrations.

811

812 **Fig. 9** Structure of the organic carbon found in Y000593 revealed by Energy Electron Loss  
813 Spectroscopy (EELS). **(a)** Carbon K-edge EELS reference spectra for calcite, graphite, amorphous

814 carbon and diamond, with the dashed lines showing the  $1s \rightarrow \pi^*$  electronic transition at  $\sim 285$  eV  
815 and the  $1s \rightarrow \sigma^*$  exciton at  $\sim 292$  eV for graphite. **(b)** Carbon K-edge spectra measured from the  
816 red boxes in areas a and b of FIB lamellae- 3 closely match the amorphous carbon reference  
817 spectrum shown in **(a)**. EELS Carbon K-edge reference spectra were taken from (Garvie and Busek  
818 2006).

819

820 **Fig. 10** Schematic showing the sequence of events affecting Yamato 000593 and the co-magmatic  
821 Nakhla meteorites in the Martian subsurface with development of the olivine microtextures  
822 through time. Starting with the planetary scale events (left hand panel) T<sub>1</sub> shows condensation of  
823 exogenous organics onto the Martian surface with permafrost in subsurface clinopyroxenites. T<sub>2</sub>  
824 shows formation of an impact crater with fracturing and brecciation of the crust, impact heating  
825 causing melting of the permafrost, generation of volatile organics from impact gases and possible  
826 siderite decomposition. T<sub>3</sub> shows continued hydrothermal alteration with iddingsite formation and  
827 organic redistribution due to fluid circulation and possible organic carbon synthesis via Fischer-  
828 Tropsch type processes. At the microtextural scale (right hand panel) T<sub>1</sub> shows fresh unaltered  
829 olivines in the mafic subsurface of Mars followed by an impact event at T<sub>2</sub> that causes fracturing  
830 and micro-brecciation of the olivines, and then at T<sub>3</sub> the formation of aqueous alteration products  
831 (iddingsite, dark yellow) and redistribution of organic carbon (red) via hydrothermal circulation.  
832 Age constraints (1) from Borg and Drake (2005). Relative location of the Nakhla meteorites and  
833 hydrothermal model from Bridges and Schwenzer (2012). GV = Governador Valadares meteorite.

#### 834 SUPPLEMENTARY

835 **Fig. S1.** Chemistry of iddingsite alteration in fractured olivine (grain 5, area 3) of martian meteorite  
836 Y000593 characterized by NanoSIMS ion mapping of the boxed area (yellow) in the left hand

837 BSE (back scatter electron) image. Again the brecciated morphology of the olivine crystal margins  
838 is clearly seen in the S<sup>-</sup> map, while organic material (measured as CN<sup>-</sup>/C<sup>-</sup> to exclude any possible  
839 contamination from resin) also occurs within most of the iddingsite alteration textures at the olivine  
840 crystal margin. Intensity calibration bars are expressed as total counts for FeO<sup>-</sup>, O<sup>-</sup> and S<sup>-</sup>, and as  
841 a simple ratio for CN<sup>-</sup>/C<sup>-</sup>.

842

843 **Fig. S2.** Data from a FIB lamella cut from a resin impregnated chip of Y000593 to document the  
844 occurrence of resin in the sample **(a)** Back scatter electron image of the site where the FIB lamella  
845 was cut (red line) parallel to the margins of an iddingsite filled fracture; **(b)** Darkfield STEM  
846 overview image of the FIB lamella that mainly consists of olivine with a diagonal fracture  
847 containing resin introduced during sample preparation, dashed boxed shows area selected for  
848 elemental mapping. The TEM-EDS maps clearly show a correlation between the elements C and  
849 chlorine, and furthermore an EDS spectra measured from the yellow boxed area shows a clear Cl  
850 peak. Scale bar is 5 μm, the brightness/intensity of the colour scale reflects the relative  
851 concentration of the individual elements.

852

853

854

855

856

857

858

859

860

861